REPORT DOCUMENTATION PAGE

Form Approved
OMB No. 0704-0188

Public reporting burden for this collection of information is estimated to average 1 hour per response, including the time for reviewing instructions, searching existing data sources, gathering and maintaining the data needed, and completing and reviewing this collection of information. Send comments regarding this burden estimate or any other aspect of this collection of information, including suggestions for reducing this burden to Department of Defense, Washington Headquarters Services, Directorate for Information Operations and Reports (0704-0188), 1215 Jefferson Davis Highway, Suite 1204, Arlington, VA 22202-4302. Respondents should be aware that notwithstanding any other provision of law, no person shall be subject to any penalty for failing to comply with a collection of information if it does not display a currently valid OMB control number. **PLEASE DO NOT RETURN YOUR FORM TO THE ABOVE ADDRESS.**

1. REPORT DATE *(DD-MM-YYYY)*	2. REPORT TYPE	3. DATES COVERED *(From - To)*
30-03-2007	Final Performance Report	02-15-2004 to 31-12-2006

4. TITLE AND SUBTITLE	
SparkJet Actuators for Flow Control	**5a. CONTRACT NUMBER**
	5b. GRANT NUMBER FA9550-04-1-0095
	5c. PROGRAM ELEMENT NUMBER

6. AUTHOR(S)	
B.Z. Cybyk, D.H. Simon, H.B. Land III, J.T. Wilkerson	**5d. PROJECT NUMBER**
	5e. TASK NUMBER JHU/APL Task FG1HR
	5f. WORK UNIT NUMBER

7. PERFORMING ORGANIZATION NAME(S) AND ADDRESS(ES)	8. PERFORMING ORGANIZATION REPORT NUMBER
The Johns Hopkins University Applied Physics Laboratory 11100 Johns Hopkins Road Laurel, MD 20723-6099	GED-R-07-7606

9. SPONSORING / MONITORING AGENCY NAME(S) AND ADDRESS(ES)	10. SPONSOR/MONITOR'S ACRONYM(S)
USAF, AFRL AFOSR/NA 875 N. Randolph St., Rm. 3112 Arlington, VA 22203 *Dr John Schmisseur*	 AFRL-SR-AR-TR-07-0133

12. DISTRIBUTION / AVAILABILITY STATEMENT
Unlimited

Approved for Public Release — Distribution A

13. SUPPLEMENTARY NOTES

14. ABSTRACT
Effective manipulation of a flow field can lead to a number of significant benefits to aerospace vehicle systems, including enhanced performance, maneuverability, payload and range, as well as lowered overall cost. These macro benefits are directly achievable through the application of flow-control technology on the micro scale. Practical application of active flow control is dependent upon the development of robust actuators that are reliable, low cost, and responsive. An example of promising actuator technology for supersonic flow applications is the SparkJet actuator under development at The Johns Hopkins University Applied Physics Laboratory. The SparkJet has demonstrated the ability to produce a synthetic jet with high exhaust velocities, and hence holds the promise of manipulating high-speed flows without moving aerodynamic structures. Practical application of the SparkJet technology will require the development and demonstration of distributed actuator arrays.

15. SUBJECT TERMS
Micro-adaptive flow control, flow control actuators, SparkJet actuator, supersonic flows

16. SECURITY CLASSIFICATION OF: (U)			17. LIMITATION OF ABSTRACT	18. NUMBER OF PAGES	19a. NAME OF RESPONSIBLE PERSON B.Z. Cybyk
a. REPORT (U)	b. ABSTRACT (U)	c. THIS PAGE (U)		26	19b. TELEPHONE NUMBER *(include area code)* 240-228-7624

Standard Form 298 (Rev. 8-98)
Prescribed by ANSI Std. Z39.18

Final Report

SparkJet Actuators for Flow Control

March 2007

B.Z. Cybyk, D.H. Simon, H.B. Land III, J.T. Wilkerson
The Johns Hopkins University Applied Physics Laboratory
11100 Johns Hopkins Road
Laurel, MD 20723-6099

20070426204

TABLE OF CONTENTS

SparkJet Actuators for Flow Control

Executive Summary

The generation of plasmadynamic discharges for near-surface aerodynamic applications holds the promise of providing rapid and flexible steering control for advanced high-speed flight vehicles. Effective manipulation of a flow field can lead to a number of significant benefits to aerospace vehicle systems, including enhanced performance, maneuverability, payload and range, as well as lowered overall cost. These macro benefits are directly achievable through the application of flow control technology to impact fluid phenomena such as transition, turbulence, and flow separation on a micro-scale. Practical application of active flow control is dependent upon the development of robust actuators.

Under AFOSR sponsorship (AFOSR Grant Number FA9550-04-1-0095), The Johns Hopkins University Applied Physics Laboratory (JHU/APL) is investigating a promising cavity device for high-speed flow control called the SparkJet actuator. This actuator, which produces a synthetic jet with high exhaust velocities, holds the promise of manipulating high-speed flows without active mechanical components. Computational and experimental techniques are being used to investigate the operating characteristics of this cavity device. Computational Fluid Dynamics (CFD) modeling is used to investigate the fundamental physics and flow interactions within and near the device. CFD parametric studies characterized the performance attributes of the mm-scale device as a function of orifice size, chamber volume, and energy deposited. Ongoing experimental efforts to assess the latest actuator design include the application of high-resolution particle image velocimetry to quantify quiescent air operation, and the use of a miniaturized thrust stand to measure SparkJet impulse bit data and to determine an optimal duty cycle. Both data sets are being used to calibrate the CFD computations and to determine a confidence level in the prediction capability.

The SparkJet actuator has demonstrated the ability to produce a synthetic jet with high exhaust velocities and hence holds the promise of manipulating high-speed flows without moving aerodynamic structures. Existing piezo-mechanical synthetic jet devices, which operate with much lower exhaust velocities, have been shown to be effective for low-speed flow control, but they cannot develop sufficient driving pressure to penetrate supersonic boundary layers. The envisioned long-term payoff is the development of a micro-actuated SparkJet flow control system for enhanced aerodynamic performance of small, highly maneuverable, high-speed vehicles.

Personnel Involved (Duration of Grant)
JHU/APL: Bohdan Z. Cybyk (aerospace engineer), Kenneth R. Grossman (electrical engineer), H. Bruce Land III (electrical engineer), Daniel H. Simon (aerospace engineer), Jordan Wilkerson (mechanical engineer)

JHU: Jun Chen, post-doc, Mechanical Engineering Department (Oct 2004 through Jul 2005)

Publications

Cybyk, B.Z., Wilkerson, J.T., and Grossman, K.R., "Performance Characteristics of the SparkJet Flow Control Actuator," AIAA Paper No. 04-2131, 2nd AIAA Flow Control Conference, Portland, OR, June, 2004.

Cybyk, B.Z., Grossman, K.R., Wilkerson, J.T., Chen, J. and Katz, J., "Single-Pulse Performance of the SparkJet Flow Control Actuator," AIAA Paper 05-0401, 43rd AIAA Aerospace Sciences Meeting and Exhibit, Reno, NV, January 2005.

Cybyk, B.Z., Simon, D.H., Land, H.B., Chen, J. and Katz, J., "Experimental Characterization of a Supersonic Flow Control Actuator," AIAA Paper 06-0478, 44th AIAA Aerospace Sciences Meeting and Exhibit, Reno, NV, January 2006.

Cybyk, B.Z., Wilkerson, J.T., and Simon, D.H., "Enabling High-Fidelity Modeling of a High-Speed Flow Control Actuator Array," AIAA Paper 06-8034, 14th AIAA/AHI Space Planes and Hypersonic Systems and Technologies Conference, Canberra, Australia, November 2006.

1. Introduction

Active flow control is regarded as an enabling technology for many advanced air vehicle concepts under consideration. Effective manipulation of a flow field can lead to a number of significant benefits for aerospace vehicles, including enhanced performance, maneuverability, payload, and range, as well as lowered overall cost. These macro benefits are directly achievable through the application of flow-control technology to impact fluid phenomena such as transition, turbulence, and flow separation on the micro scale.[1,2,3,4,5,6] Organizations such as the United States Air Force and NASA continue to investigate the potential advantages of active flow control over more traditional aerodynamic techniques.[7,8] A need exists for a robust flow control actuator that is capable of penetrating supersonic boundary layers.

Several classes of micro-actuators are under investigation for flow control applications associated with aerospace vehicle systems. Most use mechanical deflection of control surfaces, mass injection, or synthetic jets. Others manipulate electromagnetic fields in an attempt to control flow.[9,10,11] Mechanical actuators include electroactive polymers, shape memory alloys, electro-active ceramics, and Micro-Electro-Mechanical Systems (MEMS) flaps.[12,13,14] These actuators control flow by movement of a control surface or manipulation of surface texture. Mass injection devices include combustion-driven jet actuators, which burn a gaseous fuel-air mixture.[15] A small chamber is filled with a combustible mixture and then ignited, resulting in high pressures inside the chamber and mass expulsion through the chamber orifice. Synthetic jet actuators are fluidic control devices.[16] They typically use a piezo-electric diaphragm in a cavity opposite an orifice. The oscillatory motion of the diaphragm alternately decreases the cavity volume, expelling gas, then increases the cavity volume, refilling the cavity with gas. Synthetic jet actuators transfer momentum into the external system without net mass transfer.

Each of the aforementioned actuators has significant limitations for application to supersonic flow control. Shape memory alloys have high power requirements, poor cycle life, and are not readily scalable. Electro-active ceramics produce very small strain. MEMS devices are highly complex and expensive. Mass injection devices require fuel sources and mechanical valving. Finally, diaphragm-driven synthetic jets produce relatively low jet velocities. Under Air Force Office of Scientific Research (AFOSR) sponsorship, The Johns Hopkins University Applied Physics Laboratory (JHU/APL) is investigating a system for high-speed flow control called the SparkJet. The SparkJet, which produces a synthetic jet with high exhaust velocities, holds the promise of manipulating high-speed flows without moving structures. The overall objective of the three-year research grant is to develop, assess, and mature the SparkJet actuator concept for active supersonic flow control. Computational and experimental techniques are being used concurrently to quantify the performance characteristics of the pulsating flow from a cavity version of the device. Analyses and demonstrations performed to date indicate that the SparkJet concept has the potential of generating exhaust streams that can penetrate supersonic (as well as subsonic) boundary layers without the need for active mechanical components.

2. Nomenclature

D = distance between collocated actuators
D_{ch} = chamber diameter

D_{ex}	=	chamber orifice diameter
E	=	chamber internal energy, Young's modulus
$f_{d,eff}$	=	resonant frequency
I	=	light intensity
I_{bit}	=	impulse bit
k	=	spring constant
L	=	beam length
M	=	Mach number
m	=	mass
m_{eff}	=	effective system mass
$m_{0,eff}$	=	initial effective mass
Q	=	energy deposited
T	=	temperature
t	=	time, beam thickness
V_{ch}	=	chamber volume
V_i	=	capacitor potential
V_y	=	velocity in the y direction
w	=	beam width
x	=	amplitude, distance
y	=	chamber axis
α	=	flow angle
λ	=	wavelength of the laser source
$\omega_{n,eff}$	=	effective natural frequency
$\omega_{d,eff}$	=	damped effective natural frequency
ξ_{eff}	=	effective damping coefficient

3. Actuator Description and Operation

The SparkJet is a completely solid-state device that consists of a small chamber with electrodes and a discharge orifice.[17] High chamber pressure is generated by rapidly heating the gas inside the SparkJet using an electrical discharge. The pressure is relieved by exhausting the heated air through an orifice.

A single cycle of SparkJet operation consists of three distinct stages:[18] energy deposition, discharge, and recovery (Fig. 1). The cycle is repeated continuously to create a synthetic jet capable of causing a macro-scale flow effect when positioned in a region of high receptivity. The device transfers momentum with the external surroundings without net mass transfer. The amount of mass expelled during each cycle is large compared to that of piezo-electric devices.

In active flow control, disturbances produced by such a cavity device are used to take advantage of fluid phenomena such as
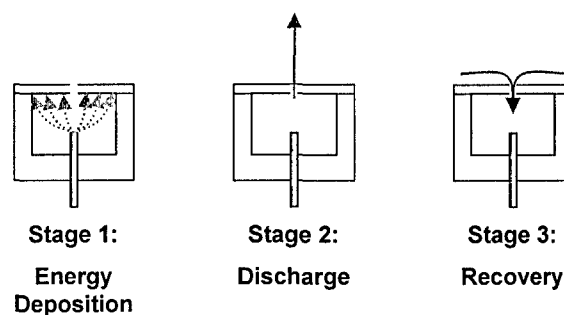

Stage 1:
Energy
Deposition

Stage 2:
Discharge

Stage 3:
Recovery

Figure 1. SparkJet cycle.

6

transition, turbulence, and flow separation. Conversely, these disturbances can also be used to study the development of such phenomena. For example, electrical discharges in a recessed cavity have been used in experiments to generate artificial disturbances for the study of laminar-to-turbulent transition.[19,20] The disturbance frequencies were at levels typically needed for active flow control.

Figure 2 presents a cross section of the SparkJet chamber. The device consists of a ceramic component with a cathode that determines the chamber volume. The ceramic component is inserted between a stainless steel holder and a threaded brass cap with a jewel orifice installed in the face (Fig. 3). This SparkJet design has several significant advantages over previous designs: it is more robust, allowing for reliable testing; it provides a precise volume and orifice; and it allows for greater flexibility in testing and ease of use.
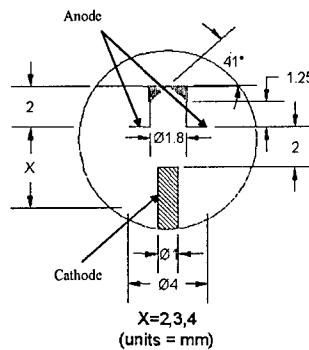

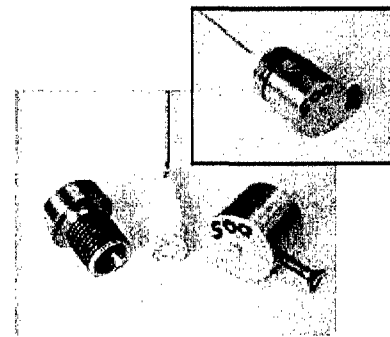Figure 2. Schematic of the two-electrode SparkJet actuator.

Figure 3. Individual SparkJet components (inset shows assembled unit).

The global characteristics of a single discharge cycle have been determined using analytical, computational, and experimental methods. These efforts are discussed in the next three sections.

4. First-Order Model

A first-order model of the SparkJet operation has been developed using the energy equation applied to a control volume enveloping the chamber:

$$\iiint_V \dot{q}\rho\,dV - \iint_S \dot{q}'\,dS - \iint_S P\vec{U}\cdot d\vec{S} = \iiint_V \frac{\partial}{\partial t}\left[\rho\left(e+\frac{U^2}{2}\right)\right]dV + \iint_S \rho\left(e+\frac{U^2}{2}\right)\vec{U}\cdot d\vec{S} \tag{1}$$

7

In this equation $\dot{q}$ = heat added per unit mass to the control volume and $\dot{q}'$ = heat lost from the control volume through its surface.

A detailed discussion of this analytical model can be found in Appendix A as well as in Grossman et al. (2003). Using this analytical model, basic operating characteristics of the SparkJet device can be discerned. For instance, many aspects of the operation are controlled by the ratio of the energy deposited (Q) to the initial internal energy (E) of the gas within the control volume. As seen in Fig. 4(a), the velocity of the discharge jet (U_{ex}) ranges from approximately 600 to 950 m/s at the beginning of the fluid discharge stage for sonic orifice flow. The amount of the initial mass expelled and the fraction of deposited energy expelled are shown in Fig. 4(b) and Fig. 4(c), respectively. At high-energy deposition levels, the SparkJet is very efficient in transferring electrical energy into kinetic energy of the injected mass.
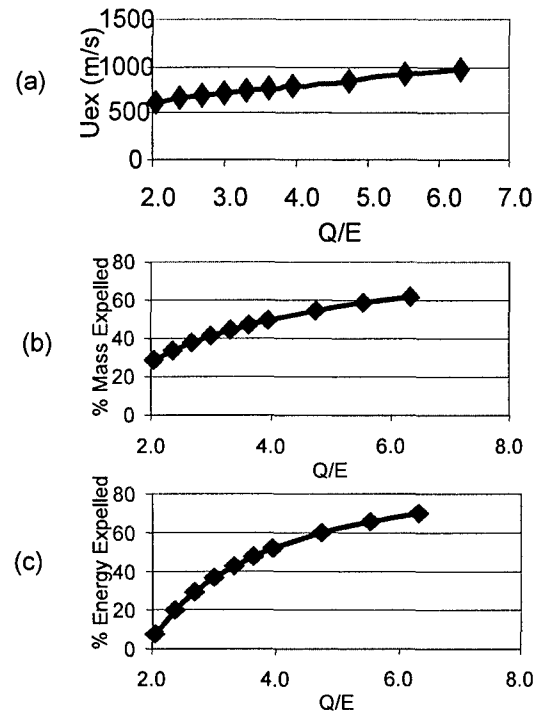

Figure 4. Effect of energy deposition on SparkJet operating characteristics

5. Computational Predictions

Both 2D and 3D time-dependent Navier-Stokes calculations of the SparkJet operation have been conducted using the commercial Computational Fluid Dynamics flow solver CFD++. Figure 5 presents a 1200 μs time history of the temperature and velocity fields predicted by CFD within and above the SparkJet chamber. In this figure, the color scale progresses from blue (min) to red (max) corresponding to temperatures from 300 to 1000 K and velocities from -100 to 400 m/sec. The rectangular zone that represents the annular energy deposition region in 3D is visible in the t=0 snapshot. The first ~1000 μs period represents the SparkJet discharge stage (stage 2) of device operation, followed by the first 200 μs of the recovery stage (stage 3). Figure 6 presents the time histories of average (area-weighted) temperature and velocity across the orifice exit plane. Note that substantial fluctuations exist in the averaged quantities across the orifice exit plane.

A parametric CFD study was conducted to quantify the sensitivities of single-pulse device performance on orifice diameter, D_{ex}, chamber volume, V_{ch}, and energy deposited, Q, for the SparkJet firing into quiescent air. The range of parameters investigated as part of the study included orifice diameters of 5, 13, and 26 mil (0.127, 0.33, 0.66 mm), chamber volumes of 2.877E-8, 4.056E-8, and 5.234E-8 m^3, and energy deposition values of 0.0126, 0.0302, 0.0478, and 0.0654 J. The effects of increasing Q on total impulse are shown Fig. 7. With a constant chamber volume, increasing Q increases the total impulse. Furthermore, a larger diameter orifice produces a larger impulse, indicating that viscous effects play a significant role for the range of device sizes investigated. Therefore, a SparkJet can be calibrated for a specific application by

varying the energy deposition and orifice diameter. CFD simulations of fully-developed Mach 3 flow over a surface-mounted SparkJet indicate that a single discharge is sufficient to penetrate a supersonic boundary layer.[21] SparkJet operation in synthetic jet mode (with target frequencies up to 1 KHz) significantly increases the effect of the effluent on the surroundings.
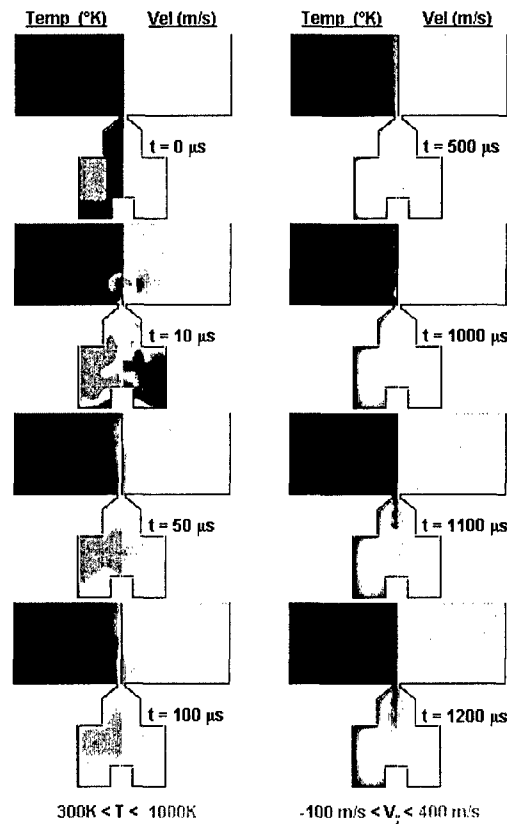

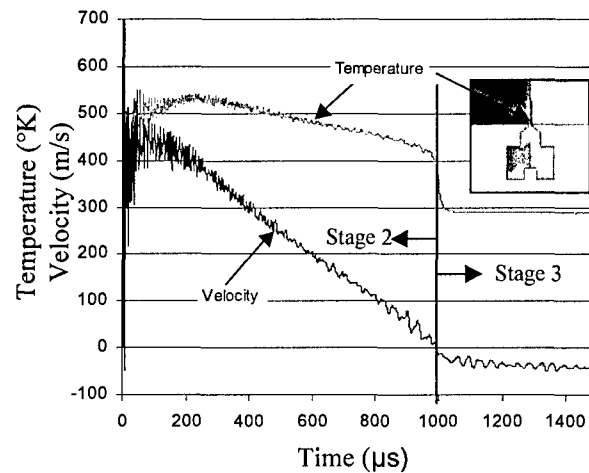Figure 5. Temperature and velocity time histories predicted by CFD after single energy deposition pulse at t=0.

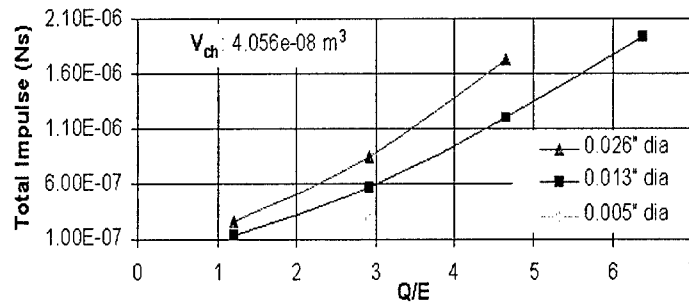Figure 6. Average temperature and velocity time histories at the orifice exit.

9

Figure 7. Effect of energy deposition on impulse.

6. Experimental Results

Time-sequenced Schlieren photographs, shown in Fig. 8, provide visual verification of device operation. Although it is possible to obtain some quantitative data from Schlieren photographs, the inherent uncertainty in the results is relatively high. In order to acquire higher accuracy data, detailed experimental analyses of the SparkJet flow characteristics are being explored using advanced flow visualization techniques. Device operation is being examined using high-resolution particle image velocimetry at The Laboratory for Experimental Fluid Dynamics at the Johns Hopkins University. Furthermore, a miniaturized thrust stand designed to support the development of a micro-Pulsed Plasma Thruster concept under JHU/APL IR&D funding is being used to measure SparkJet impulse bit data and to determine an optimal duty cycle. Both data sets will be used to calibrate the CFD simulations and to determine a confidence level in the prediction capability.

6.1 Actuator Redesign

Initial SparkJet proof-of-principle designs and experiments were based upon the simple two-electrode design shown in Figs. 2 and 3. While a two-electrode device is relatively simple mechanically and electronically, it presents issues operationally. Operation is dependent upon the spontaneous breakdown of the air for creation of the spark. The breakdown potential will vary with oxidation of the electrodes, the electrode gap, and the gas pressure within the chamber. Since the breakdown is spontaneous, coordinating the breakdown with diagnostic equipment is difficult.
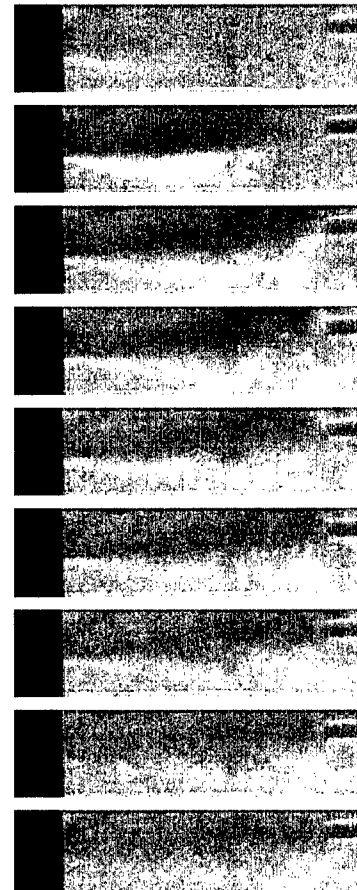

Figure 8. Schlieren photographs of a SparkJet discharge.

10

Triggering requirements for high-resolution PIV studies (discussed in the next section) necessitated a redesign. The design has now transitioned to a three-electrode configuration (Fig. 9) to reduce the size of the power supply, allow easy synchronization, and increase reproducibility and reliability. The new devices are machined from Macor, a machinable glass ceramic from Corning. Macor was chosen because of its insulative properties and the ease with which it can be machined with normal tooling, enabling mass production as cast units.

Figure 9. Individual SparkJet unit (with electronics and power supply).

The ability to control the timing and synchronization of the discharge is inherent in the three-electrode design, allowing experimental measurements to be timed precisely with device operation. The three-electrode device has a ground electrode, a main electrode, and a trigger electrode. Device discharge occurs only when the trigger voltage is activated. Thus, the voltage and energy in the discharge can be adjusted over a wide range without causing spontaneous discharge to occur. The trigger electrode produces a kilovolt pulse that ionizes the air gap, allowing the energy from the main capacitor to discharge between the main electrodes. The main capacitor needs to be charged only to hundreds of volts rather than the kilovolts needed in the two-electrode design, resulting in significant savings in power supply cost, weight, and volume.
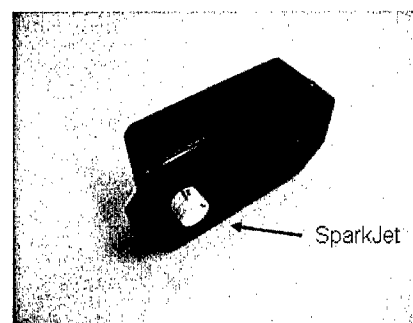
6.2 High-Resolution PIV

6.2.1 Setup and Instrumentation

In order to obtain non-intrusive field measurements needed to characterize the SparkJet discharge, a high-resolution PIV system is employed.[22] The SparkJet device is mounted inside and on the top center of an acrylic chamber constructed specifically for this study. The test chamber, shown in Figs. 10 and 11, has inner dimensions of 375(L) × 250(W) × 350(H) mm. It sits on an optical frame with PIV hardware deployed from the outside.
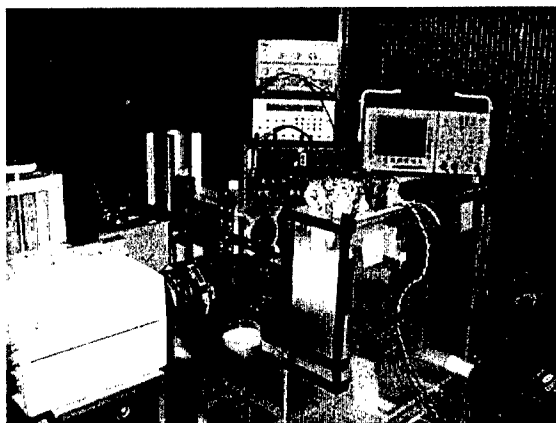
The test chamber is seeded with smoke particles (1-3 μm in diameter) generated by a Lite F/X fog machine from an inlet in the bottom corner of the chamber. A vertical baffle plate is set up inside the chamber to prevent big smoke particles from entering the sample area. A small electrical fan with DC speed control introduces a weak circulating flow pattern inside the chamber to agitate the smoke particles. Only small particles enter the sample area while large particles are stranded near the bottom and far from the sample area. The residual flow caused

Figure 10. Experimental setup for micro-PIV studies of the SparkJet device.

11

by the agitation process is very small compared to the jet velocity and thus is ignored.   The smoke generator ejects smoke particles into the test chamber only during the experiment preparation stage. Preliminary tests show that the smoke particles remain uniformly suspended for approximately 20 minutes. The internal chamber of the SparkJet device is not seeded with particles.

The beam from the PIV light source, a dual-head Nd-YAG laser (532 nm, 120 mJ/pulse maximum energy), is expanded to a 500 μm thick sheet along the central x_1-x_2 plane. The 25 $\times$ 25 mm sample area is located directly underneath the jet exit. The images are recorded using a Kodak ES-4.0 digital camera, with a resolution of 2048 $\times$ 2048 pixels, and a Nikon 105mm Nikkor lens. The camera is mounted on a 3D translation stage for fine position adjustment. The power supply of the SparkJet device, the laser and camera controllers, and the data acquisition system are all synchronized with each other, as shown in Fig. 12.

The camera records two consecutively exposed images on two separate frames. The time interval between laser pulses ranges from 2 to 10 μs, depending on the timing phase of the jet evolution, and is too short to be controlled accurately by only setting the timing of firing flash lamps. Instead, the flash lamps of the two lasers are fired at the same time, and the delay between the two laser pulses is established by triggering the Q-switches of the laser heads at different times.[23] Since there are slight variations in the response of the two laser heads to the trigger signal, the exact laser timing is monitored using a fast-response photodiode connected to a 2.5 GS/s oscilloscope. The trigger signals for the flash lamps and Q-switches are generated by a 4-channel Stanford Research Delay Generator. This setup produces a timing sequence of laser pulses with an accuracy of 20 nanoseconds.
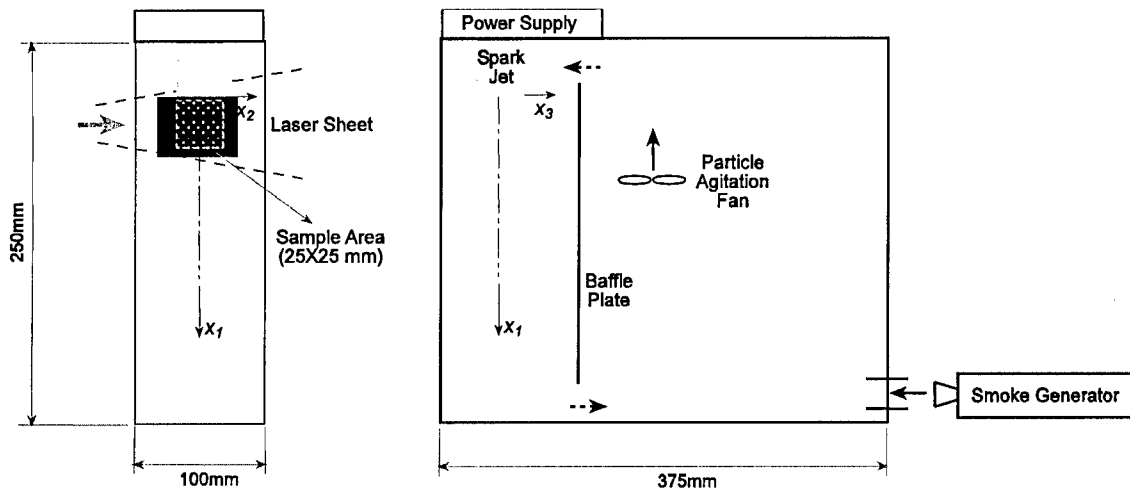

Figure 11. Schematic of the SparkJet test chamber. Front view (left), side view (right).
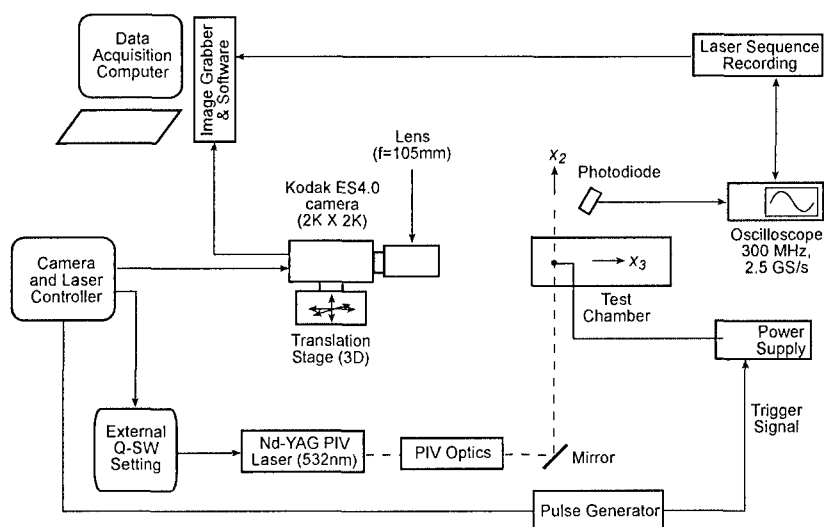
Figure 12. Schematic diagram of the PIV instrumentation system.

6.2.2 Data Processing

The edge portion of the acquired images is contaminated by surface reflection and is discarded before data processing. The data processing consists of image enhancement, followed by cross-correlation analysis to determine the velocity distributions.[24,25,26] The size of the interrogation window is 48 × 48 pixels. With 50% overlap, the vector spacing is 300 μm. A total of 63 × 75 vectors are obtained from each image pair.

6.2.3 Observations and Results

The SparkJet device being investigated has an orifice diameter of D_{ex} = 0.33 mm (0.013 inches) and a chamber volume V_{ch} = 4.228E-8 m^3. The capacitor potential to initiate the spark discharge is V_i = 1000 volts. The SparkJet is operated at 0.2 Hz to examine the characteristics of a single pulse. Figure 13 presents typical PIV images from two different SparkJet discharges under the same experimental conditions. The flow structure is well visualized because the ambient air within the test chamber contains enough smoke particles to be seen in the recorded images, while the jet core is dark due to insufficient seeding. The jet structure exhibits a good repeatability, making it feasible to study the evolution of the jet through repeated measurements of different SparkJet discharges.

Figure 14 shows the resolved velocity fields at different snapshots in time as well as the vorticity components calculated using finite differencing. All these results are considered instantaneous due to the very short laser pulse (on the order of 10 ns) and no ensemble averaging is applied. At t = 0, the spark is ready to discharge; no flow motion is detected. After the spark discharges, a puff of hot plasma is ejected into the PIV test chamber through the orifice. This puff propagates into the test chamber and expands in all lateral directions, introducing a strong leading vortex ring. Behind this puff, the ambient air is entrained into the wake, producing a weak trailing vortex ring. Both vortex ring structures can be seen clearly at t = 25 μs. Visible in each velocity field snapshot is the wave front propagation at t = 25, 50, 75, and 150 μs when the

13

air at the puff interface is significantly compressed. At $t = $ ~200 μs (not shown), the measured velocity of the entrained fluid reaches a peak value of 100 m/s. The actual speed at the jet core is believed to be much higher due to insufficient seeding in the core area and the spatial-averaging effect of the PIV velocity measurements. As the mixing between the jet and the ambient air continues, increasingly complex vorticity patterns are produced. At $t = $ 500 μs, the jet penetrates the entire depth of the field of view (25 mm). The jet continues to propagate further into the test chamber as the velocity magnitudes decay.
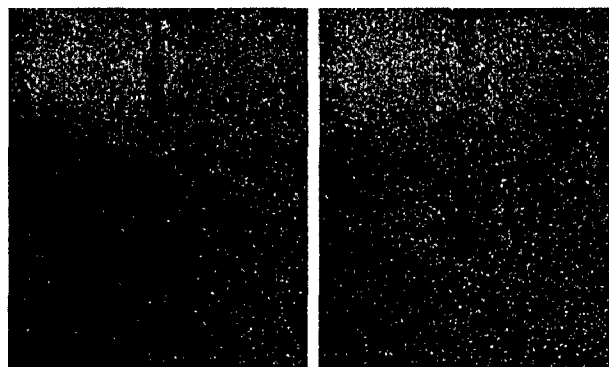

Figure 13. Particle images of separate SparkJet discharges (t = 200 μs).

6.2.4 Lessons Learned

Characterization of the unique SparkJet device using PIV has proven to be challenging. The primary hurdle is the proper seeding of the internal SparkJet chamber. In most previous PIV investigations of jet flows,[27] both the emanating jet and the ambient fluid are seeded appropriately. In the present study, only the ambient fluid has been seeded because the chamber inside the SparkJet device is very small and a tiny orifice is the only access point. Consequently, the actual high-speed jet core flow has yet to be measured. In an attempt to overcome this problem without modifying the geometry of device, we are exploring the possibility of seeding the spark chamber directly by injecting a very small amount (0.005ml) of methanol solution with SiO_2 particles (mean diameter 850 nm) through the orifice. The volatilizing methanol is expected to leave only SiO_2 particles in the spark chamber. Once the seeding problem is solved, PIV measurements will be repeated as needed for statistical analysis.

Strong electromagnetic interference (EMI) from the SparkJet discharge had been an issue with the sensitive control apparatus for the Nd-YAG laser and camera control. False triggers were common and had prevented collection of quantifiable velocity data. The SparkJet power supply redesign (described previously) significantly reduced the EMI, as did shielding of the power supply enclosure using aluminum foil.

Glare emitted by the spark was also of concern because it may degrade the particle images. However, preliminary tests indicated that this undesired light is much weaker than the laser sheet. Since the adverse influence on particle images is minimal, an optical bandpass filter initially added to block the glare is no longer necessary.
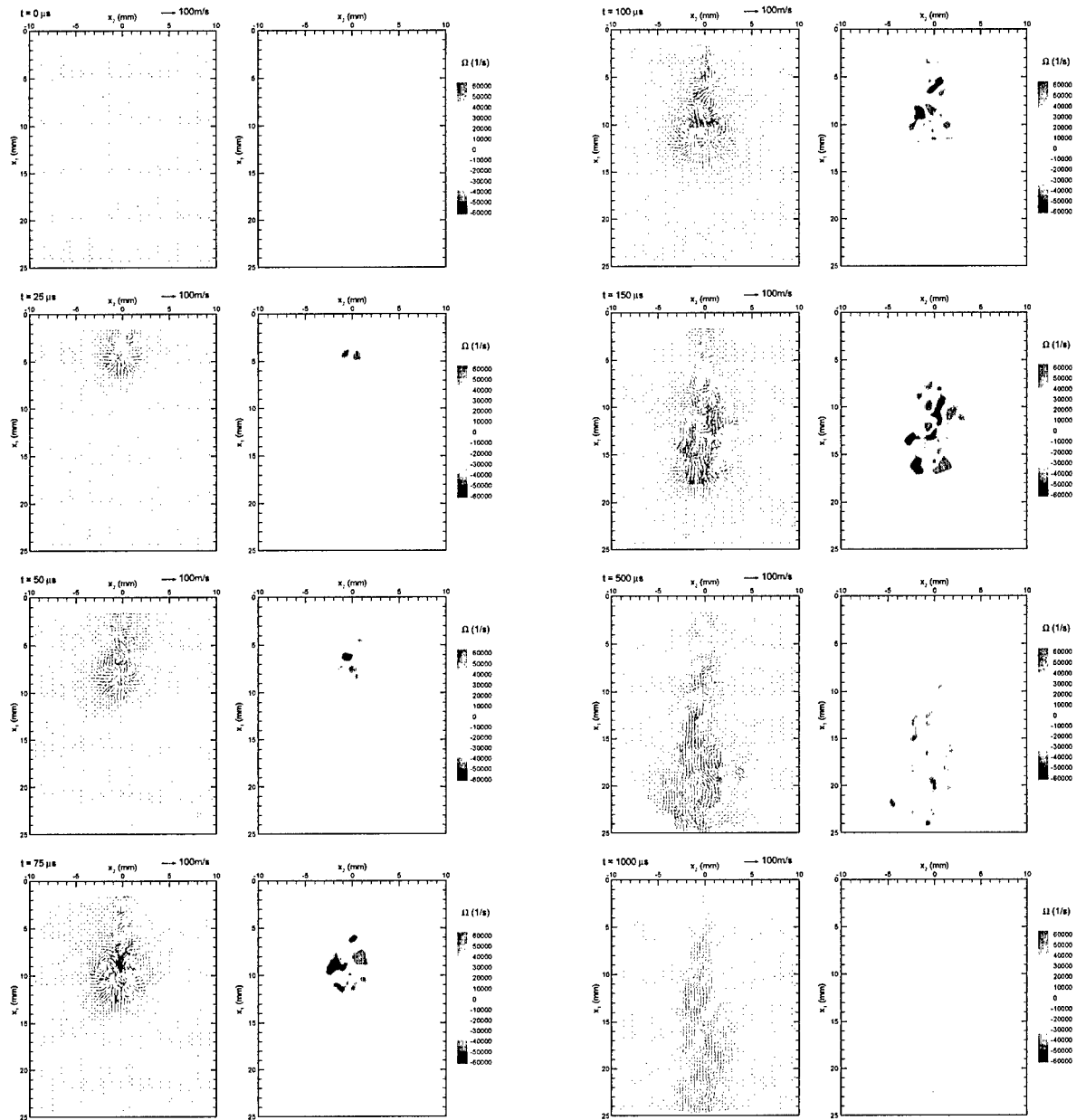
14

Figure 14. Time history of the resolved PIV velocity fields (left) and the out-of-plane component of vorticity (right).

Limitations of the available double-exposure camera have also impacted the application of PIV to the SparkJet actuator. The Kodak ES-4.0 camera is capable of taking PIV images with a minimum laser pulse delay of 1 μs for cross-correlation analysis. At present, the JHU Laboratory of Experimental Fluid Dynamics is purchasing a new state-of-the-art PIV system with digital recording capability (minimum laser pulse delay 200 ns) that is expected to meet SparkJet analysis requirements.

15

6.3 Miniaturized Thrust Stand

A miniaturized thrust stand is under development at JHU/APL to assist with the characterization of various micropropulsion devices. The stand, pictured in Fig. 15, consists of a small 3 x 3 cm platform suspended by four rigid cantilever beams. The platform and beams are fabricated from a single sheet of stainless steel shim stock. This metal structure is oriented vertically and clamped at the top and bottom in a Lexan® fixture. The fixture is mounted on top of a custom-built miniature shaker table that is used to calibrate the thrust stand. The shaker table is driven by a single piezoelectric linear actuator from ThorLabs. A SparkJet actuator can be bonded directly to this movable 3 x 3 cm platform. Electrical power is carried to the device by several strands of thin magnet wire (small gauge wire with an electrically insulating shellac coating). Impulse imparted from the actuator causes the platform to vibrate ever so slightly.
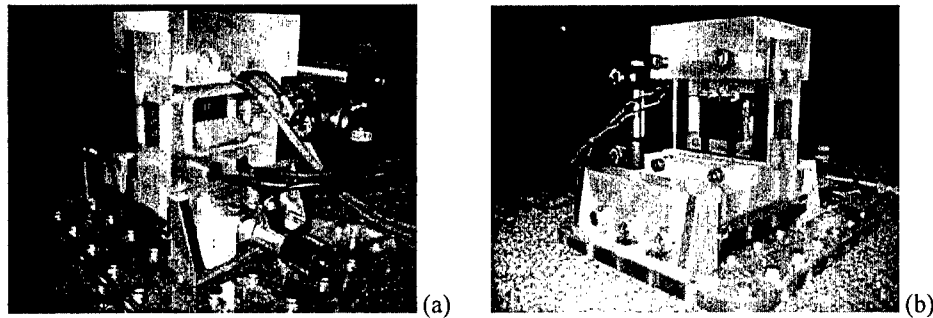

Figure 15. JHU/APL miniature thrust stand. (a) Front. (b) Back.

To measure the amplitude of these vibrations a Michaelson interferometer setup is employed. As illustrated in Fig. 16, the beam from a 4.5 mW, 670 nm laser diode module from ThorLabs is passed through a non-polarizing beam splitter. One portion of the beam then passes through a quartz window into the vacuum chamber, reflects off a mirror mounted on the thrust stand's moveable platform, and returns to the beam splitter. The other portion of the beam is reflected back to the beam splitter through a stationary mirror. The beam splitter then directs both beams towards a photodiode detector where they generate an interference pattern. As the position of the thrust stand platform moves, the intensity of the light at the detector varies as

$$I(t) = \frac{I_{max}}{2}\left[1 + \cos\left(\frac{4\pi x(t)}{\lambda}\right)\right] \tag{2}$$

where $x(t)$ is the position of the mirror and λ is the wavelength of the laser source. Note that the output is sinusoidal and repeats every time the platform moves by a ¼ of a wavelength. To minimize background vibrations due to environmental effects, the vacuum chamber and interferometer have been assembled on an optical bench with pneumatic isolation legs.
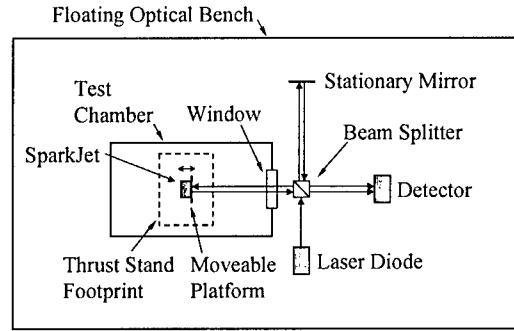
16

Floating Optical Bench

Figure 16. Laser interferometer arrangement for measuring thrust stand vibrations.

In addition to a high natural frequency, the rigid design of the steel platform and affixed beam structure is intended to have several other effects. First, the impulse imparted by a test device should cause a small deflection in each of the beams such that they behave like simple linear springs. Second, the stiffness of the beams should overwhelm that of the power supply wires and make the system simple to model. And third, the beams can limit the deflection of the platform to less than ¼ of the interferometer laser wavelength (to avoid multiple fringe patterns in the interferometer data). Larger deflections are tolerable but call for a more sophisticated data reduction process, such as that employed by Cubbin.[28]

Since the thrust stand has been designed to behave like a damped spring-mass system, its response to an applied impulse is given by

$$x(t) = e^{-\xi_{eff}\omega_{n,eff}t} \frac{I_{bit}}{m_{eff}\omega_{d,eff}} \sin\left(\omega_{d,eff}t\right) \tag{3}$$

where I_{bit} is the impulse bit, m_{eff} is the effective system mass, ξ_{eff} is the effective damping coefficient, $\omega_{n,eff}$ is the effective natural frequency, and $\omega_{d,eff} = \omega_{n,eff}\sqrt{1-\xi}$ is the damped effective natural frequency. If the damping coefficient is small, the system will essentially respond to an impulse bit with a regular sinusoidal response. The impulse bit can then be inferred by examining the amplitude of these oscillations using the approximation

$$I_{bit} \approx \Delta x \cdot m_{eff} \cdot \omega_{d,eff} \tag{4}$$

where Δx is the amplitude of the thrust stand platform vibrations. The only other system information required is the effective mass and damped natural frequency.

Each of the beams attached to the moveable platform behaves like a guided cantilever whose spring constant can be calculated according to the expression

$$k = \frac{Ewt^3}{L^3} \tag{5}$$

where E is the material Young's modulus, w is the beam width, t is the beam thickness, and L is the beam length. This system has four beams that effectively act like springs in parallel; therefore, the total spring constant of the system should be four times that of a single beam. The effective mass of the system should be close to the actual mass of the vibrating components (moveable platform, actuator, main capacitor, and mirror). The first platform and beam structure for the thrust stand was designed for an effective mass of approximately 25 g. The beam dimensions, $w = 0.25$" (6.35 mm), $t = 0.008$" (0.20 mm), and $L = 0.33$" (8.3 mm), were then designed to provide a total system spring constant of 78,270 N/m and a predicted natural frequency of 280 Hz. Moreover, this design was expected to produce vibrations with amplitudes ranging from 40 to 175 nm (a comfortable range to detect with an interferometer employing a 670 nm red laser diode) in response to impulse bits ranging from 2 to 7.5 μN-sec.

In order to accurately interpret the measurements recorded from this thrust stand, a suitable calibration process must be applied. The conventional approach to accomplish this would involve the application of a series of known loads to the platform and measurement of the associated deflections. In lieu of this procedure, an unconventional calibration process was developed for this system. As mentioned above, the thrust stand is mounted on a shaker table that can impart small vibrations controlled by a standard function generator. The resonant frequency of the platform/beam structure can be detected by varying the frequency of these vibrations and monitoring the amplitude of the platform's oscillations. Recall from Eq. 4 that this quantity alone is an important system characteristic. If a known amount of mass, Δm, is then added to the platform, the resonant frequency should drop in a predictable manner. Indeed the new resonant frequency of the system should behave as

$$f_{d,eff} = \frac{1}{2\pi} \sqrt{\frac{k}{m_{0,eff} + \Delta m}} \qquad (6)$$

where $m_{0,eff}$ is the initial effective mass (prior to the addition of any ballast). This expression can be rearranged as

$$\Delta m = \frac{k}{4\pi^2} \left(\frac{1}{f_{d,eff}^2} \right) - m_{0,eff} \qquad (7)$$

If a series of additional weights are added to the platform, Eq. 7 tells us that the total amount of added weight should vary as the inverse of the damped natural frequency squared. Therefore, these two quantities can be plotted and fit with a straight line. The y-intercept of this line reveals the effective mass of the platform/beam. The slope of this line also reveals the system spring constant. The spring constant is not explicitly required to interpret the response of the thrust stand to an impulse excitation; however, it is needed to interpret the steady platform deflection produced in response to a constant thrust.

This miniature thrust stand was used to gather preliminary impulse bit data for a single SparkJet device. The SparkJet was powered by a 220 nF capacitor rated at 1000 V. Impulse bit data was collected at five discrete voltage levels ranging from 520 to 900 V. These points correspond to energy deposition levels of 30, 40, 54, 70, and 89 mJ. A sample of this data is

shown in Fig. 17. The impulse bit data appears to vary linearly with the deposited energy. The impulse bit data exhibits some scatter at each energy level. This could be due to inherent variation in the SparkJet performance or the measurement process itself. Most encouraging, Fig. 18 shows virtually no difference in the thrust stand response between 1 Hz and 20 Hz SparkJet operation. Additional development work on the thrust stand is proceeding with the aim of reducing its uncertainty.
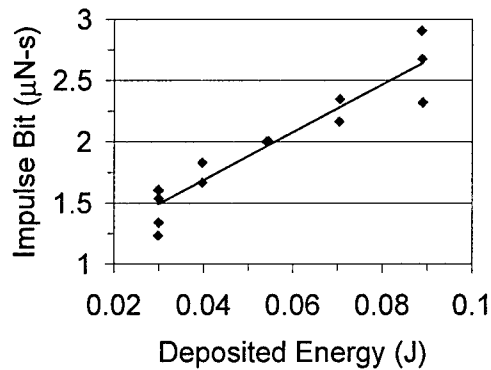
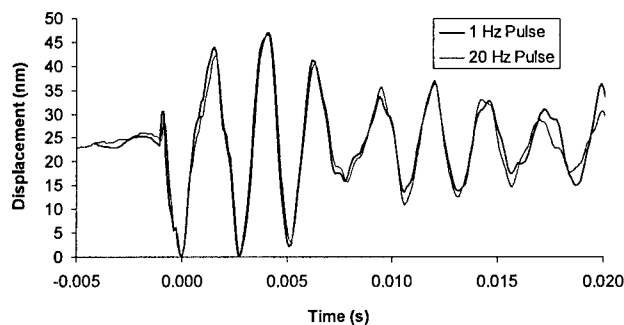Figure 17. Preliminary SparkJet impulse bit measurements.

Figure 18. Miniature thrust stand response during SparkJet operation.

7. Distributed Actuator Array Model Development

Practical application of the SparkJet technology will require the development of distributed actuator arrays. The diminutive size (120-600 µm) and high discharge velocities (400-500 m/s) of the SparkJet actuator make it very difficult to evaluate demonstration units using non-intrusive measurement techniques. Hence, modeling must be used to evaluate the effectiveness of distributed actuator arrays and their potential high-payoff applications. We have begun development of a new CFD-based computational methodology that will enable the accurate and cost-effective simulation of problems that involve distributed actuator arrays.

From a mathematical standpoint, CFD formulations will rigorously capture the flow control effects of micro-scale perturbations on the surrounding macro-scale flow, and vice versa. In reality, however, these spatially-challenged solutions require extensive computational resources (both in solution time and computer memory) that render such an approach impractical for more than a few perturbation sources operating in tandem. This is because modeling the fluid dynamics within a micro-scale perturbation source (e.g. modeling the effects of the energy deposition within the micro-actuator during a single operating cycle) substantially increases the grid and computational requirements over what is required to resolve the effects of the imparted flow disturbance on the surrounding flow. Once a detailed numerical simulation of the perturbation source exists, a fluid dynamic model of the operating cycle of the disturbance source (a virtual source) can potentially be developed and implemented via boundary conditions. This is precisely the approach that has been taken by others evaluating the effectiveness of synthetic jet actuators.[29]

Like the synthetic jet actuator, the SparkJet is also a zero net-mass-flux device. However, the SparkJet cycle adds an additional complication that invalidates the current boundary condition implementation of virtual disturbance sources. From a modeling standpoint, the problem is that the SparkJet recovery stage is dependent upon the external flow and may vary from pulse to pulse. Hence, any use of virtual SparkJet sources should capture the effect of the local boundary layer flow on the device operation. In other words, the virtual sources must "self-adapt" to the local time-varying environment.

A new parametric study is underway to evaluate the performance characteristics of collocated pulsed SparkJet actuators operating in a Mach 3 flow (Fig. 9). The purpose of this parametric study is to evaluate the effects of the distance between the actuators, D, and incoming flow angle, α, on the resultant interacting jets. SparkJet geometric characteristics (Fig. 10) and the amount of energy deposited are being held fixed. This study will provide guidelines to the development of self-adapting virtual SparkJet sources.
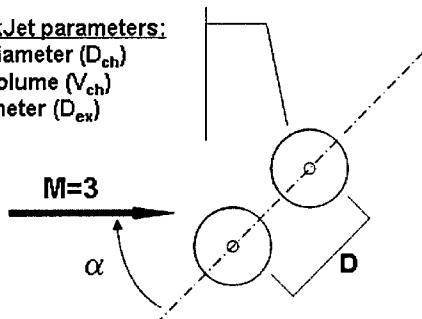

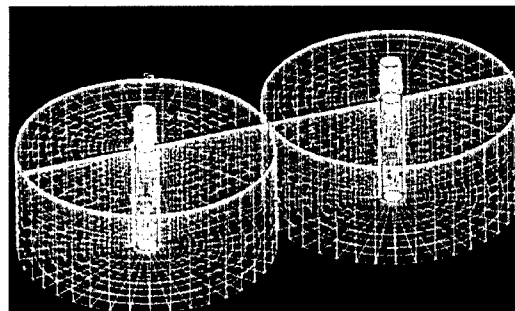Figure 9. Parametric study of collocated actuators.   Figure 10. Collocated actuator grids.

8. Summary

Effective manipulation of a flow field can lead to a number of significant benefits to aerospace vehicle systems, including enhanced performance, maneuverability, payload and range, as well as lowered overall cost. These macro benefits are directly achievable through the application of flow-control technology on the micro scale to impact fluid phenomena such as transition, turbulence, and flow separation. Practical application of active flow control is dependent upon the development of robust actuators that are reliable, low cost, responsive, and consume little power. An example of promising actuator technology for supersonic/hypersonic flow applications is the SparkJet actuator under development at JHU/APL. The SparkJet has demonstrated the ability to produce a synthetic jet with high exhaust velocities, and hence holds the promise of manipulating supersonic/hypersonic flows without moving aerodynamic structures. Practical application of the SparkJet technology will require the development and demonstration of distributed actuator arrays capable of operating in high-temperature environments.

This paper provides a synopsis of SparkJet technology development under AFOSR Grant Number FA9550-04-1-0095 and introduces an approach to the development of a computational model for the accurate and cost-effective simulation of a distributed SparkJet array operating in a macro-scale, high-speed environment. Combined computational and experimental techniques are being applied to investigate the operating characteristics of a cavity SparkJet device with the ultimate goal of developing a micro-actuated flow control system for enhanced aerodynamic performance of high-speed flight vehicles.

9. Acknowledgments

Appendix A: First-Order SparkJet Model

A first order model of the SparkJet operation has been developed using the energy equation applied to the control volume shown in Fig. A1:

$$\iiint_V \dot{q}\rho dV - \iint_S \dot{q}' dS - \iint_S P\vec{V}\cdot d\vec{S} = \iiint_V \frac{\partial}{\partial t}\left[\rho\left(e+\frac{V^2}{2}\right)\right]dV + \iint_S \rho\left(e+\frac{V^2}{2}\right)\vec{V}\cdot d\vec{S} \qquad (A.1)$$

where $\dot{q}$ is the heat added per unit mass to the control volume and $\dot{q}'$ is the heat lost from the control volume through the surface of the control volume.
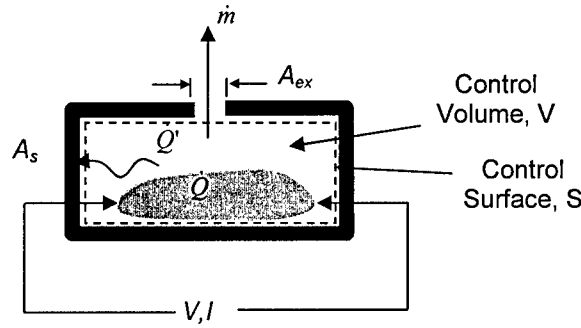

Figure A.1. SparkJet configuration.

Making the assumption of one-dimensional flow within the control volume, Eqn. (A.1) simplifies to:

$$\frac{d}{dt}(\rho e V) = \dot{Q} - \dot{Q}' A_{SURFACE} - \dot{m}h_t \qquad (A.2)$$

where ρ - density, e – internal energy, $\dot{Q}$ – rate of energy added to the control volume, $\dot{Q}'$ - rate of energy lost through the control surface (per unit area), A_S – internal surface area $\dot{m}$ - mass flow exiting control volume, and h_t – total enthalpy of flow exiting control volume.

Stage 1: Energy Deposition

Within Stage 1, an electrical discharge is created within the SparkJet volume. The energy addition is assumed to occur fast with respect to both heat and mass loss, so Eqn. (A.2) becomes:

$$\frac{d}{dt}(\rho e V) = \dot{Q} \qquad (A.3)$$

Assuming that the energy addition is constant in time, the fluid can be represented as a calorically-perfect gas and states 0 and 1 represent the conditions at the beginning and end of the first stage, Eqn. (A.3) can be written:

$$T_1 = T_0 + \frac{Q}{C_v M} \tag{A.4}$$

where M is the total mass inside the control volume and Q is the total energy added to the control volume. Since the gas density is constant during this stage, the pressure at the end of Stage 1 can be determined from:

$$P_1 = \rho_0 R \left(T_0 + \frac{Q}{C_V M} \right) \tag{A.5}$$

Hence, one can see that both the pressure and temperature of the gas within the volume are increased during Stage 1.

Stage 2: Fluid Discharge

Within Stage 2, the hot, high-pressure gas within the control volume discharges through the orifice until the point where the external and internal pressures are equalized. During this stage, no energy is added to the control volume and heat loss through the wall can be neglected, so Eqn. (A.2) can be written:

$$\frac{d}{dt}(\rho e V) = -\dot{m} h_t \tag{A.6}$$

While the discharge flow is choked at the orifice (i.e., while $P > 1.89 * P_0$), the mass flow can be related to the chamber pressure and temperature as follows:

$$\dot{m} = \frac{\left(\frac{P}{P_t}\dot{m} \right)^* P A_{ex}}{\sqrt{T}} \tag{A.7}$$

$$\text{where } \left(\frac{P}{P_t}\dot{m} \right)^* = \sqrt{\frac{\gamma}{R}} \left(\frac{\gamma+1}{2} \right)^{-\left(\frac{\gamma+1}{2(\gamma-1)} \right)}$$

If state 2 is the point in the expansion process where $P_2 = P_0$ and the expansion is assumed to occur isentropically, the time required for the fluid discharge can be determined from:

$$t_2 - t_1 = \frac{V}{\left(\frac{P}{P_t}\dot{m} \right)^* \gamma R A_{ex} \sqrt{T_1}} \left[\left(\frac{P_1}{P_2} \right)^{\frac{\gamma-1}{2\gamma}} - 1 \right] \tag{A.8}$$

23

and the temperature within the control volume can be determined as follows:

$$T_2 = T_1 \left(\frac{P_2}{P_1} \right)^{\frac{\gamma-1}{\gamma}}$$
(A.9)

In actual operation, the time required for Stage 2 will be somewhat longer than that estimated using Eqn. (A.8) since the flow will continue to discharge past the point where the orifice unchokes. At the conclusion of Stage 2, the fluid within the control volume is at ambient pressure, but with a temperature that is above ambient.

Stage 3: Recovery

During the recovery stage, heat is lost though the wall of the Sparkjet. As the heat is lost, fresh air is drawn into the control volume such that nearly ambient pressure is maintained. The amount of energy that needs to be transferred to the walls can be determined from:

$$\Delta E = \rho_2 V (e_2 - e_1)$$
(A.10)

Assuming that the heat transfer can be modeled in terms of a film coefficient:

$$h = \frac{Q'}{A_{SURFACE}(T_W - T)}$$

and assuming that a lumped heat capacity system model can be used, the temperature within the control volume can be determined from:

$$\frac{T - T_0}{T_2 - T_0} = e^{-t/\tau}$$
(A.11)

$$\text{where } \tau = \frac{C_v \rho V}{h A_{SURFACE}}$$

Thus one can see that the recovery time can be decreased (hence the operating frequency can be increased) by increasing the internal surface area of the film coefficient.

References

[1] Amitay, M., Honohan, A., Trautman, M., and Glezer, A., "Modification of the Aerodynamic Characteristics of Bluff Bodies," AIAA Paper No. 97-2004, 35th AIAA Aerospace Sciences Meeting, Reno, NV, January 1997.

[2] Amitay, M., Kibens, V., Parekh, D. E., and Glezer, A., "Flow Reattachment Dynamics over a Thick Airfoil Controlled by Synthetic Jet Actuators," AIAA Paper No. 99-1001, 37th AIAA Aerospace Sciences Meeting, Reno, NV, January 1999.

[3] Amitay, M., and Glezer, A., "Aerodynamic Flow Control of a Thick Airfoil using Synthetic Jet Actuators," ASME Paper No. FEDSM99-6922, *Proceedings of the 3rd ASME/JSME Joint Fluids Engineering Conference,* Symposium on Control of Wall-Bounded and Free-Shear Flows, edited by L. D. Kral and T. Shakouchi, San Francisco, CA, July 1999.

[4] Cattafesta, L. N. III, Garg, S., and Choudhari, M., "Active Control of Flow-Induced Cavity Resonance," AIAA Paper No. 97-1804, 4th AIAA Shear Flow Control Conference, Snowmass, CO, June 1997.

[5] Crittenden, T., Glezer, A., Funk, R., and Parekh, D. E., "Combustion-Driven Jet Actuators for Flow Control," AIAA Paper No. 01-2768, Anaheim, CA, June 2001.

[6] Pack, L. G., and Joslin, R. D., "Overview of Active Flow Control at NASA Langley Research Center," 5th SPIE Annual International Symposium on Smart Structures and Materials, San Diego, CA, March 1998.

[7] Tilmann, C. P., Kimmel, R. L., Addington, G., and Myatt, J. H., "Flow Control Research and Applications at the AFRL's Air Vehicles Directorate," AIAA Paper No. 04-2622, 2nd AIAA Flow Control Conference, Portland, OR, June 2004.

[8] Anders, S. G., Sellers, W. L. III, and Washburn, A. E., "Active Flow Control Activities at NASA Langley," AIAA Paper No. 04-2623, 2nd AIAA Flow Control Conference, Portland, OR, June 2004.

[9] Cary, A. W., Donovan, J. F., and Kral, L. D., "Flow Structure Development over an Electromagnetic Turbulence Control (EMTC) Actuator," ASME Paper No. FEDSM99-6932, *Proceedings of the 3rd ASME/JSME Joint Fluids Engineering Conference, Symposium on Control of Wall-Bounded and Free-Shear Flows,* San Francisco, CA, July 1999.

[10] Donovan, J. F., Kral, L. D., and Cary, A. W., "Numerical Simulation of a Lorentz Force Actuator," AIAA Paper No. 97-1918, 4th AIAA Shear Flow Control Conference, Snowmass, CO, June 1997.

[11] Nosenchuck, D. M., "Boundary Layer Control Using the Lorentz Force," *Proceedings of the Forum on Control of Transitional and Turbulent Flows,* ASME Fluids Engineering Conference, edited by D. E. Parekh and R. K. Agarwal, Vol. FED-237, 1996.

[12] Diez-Garias, F., and Werner, D., "Microactuator Arrays for Sublayer Control in Turbulent Boundary Layers Using the Electrokinetic Principle," AIAA Paper No. 00-0548, Reno, NV, January 2000.

[13] Kral, L. D., "Active Flow Control Technology," ASME Fluids Engineering Division Technical Brief, 1998.

[14] Pack, L. G., and Joslin, R. D., "Overview of Active Flow Control at NASA Langley Research Center," 5th SPIE Annual International Symposium on Smart Structures and Materials, San Diego, CA, March 1998.

[15] Crittenden, T., Glezer, A., Funk, R., and Parekh, D. E., "Combustion-Driven Jet Actuators for Flow Control," AIAA Paper No. 01-2768, Anaheim, CA, June 2001.

[16] Glezer, A., Allen, M., Coe, D., Smith, B., Trautman, M., and Wiltse, J., "Synthetic Jet Actuator and Application Thereof," U.S. Patent 5,758,823 (02 June 1998).

[17] Grossman, K. R., Cybyk, B. Z., and VanWie, D. M., "SparkJet Actuators for Flow Control," AIAA Paper No. 03-0057, 41st AIAA Aerospace Sciences Meeting, Reno, NV, January 2003.

[18] Cybyk, B. Z., Wilkerson, J. T., and Grossman, K. R., "Performance Characteristics of the SparkJet Flow Control Actuator," AIAA Paper No. 04-2131, 2nd AIAA Flow Control Conference, Portland, OR, June, 2004.

[19] Chokani, N., Bountin, D. S., Shiplyuk, A. N., and Maslov, A. A., "Nonlinear Aspects of Hypersonic Boundary-Layer Stability on a Porous Surface," *AIAA Journal*, Vol. 43, No. 1, January 2005, pp. 149-155.

[20] Kosinov, A. D., Maslov, A. A, and Shevelkov, S. G., "Experiments on the Stability of Supersonic Laminar Boundary Layers," *J. Fluid Mech.*, Vol. 219, 1990, pp. 621-633.

[21] Cybyk, B. Z., Simon, D. H., and Land III, H. B., "Experimental Characterization of a Supersonic Flow Control Actuator," AIAA Paper No. 06-0478, 44th AIAA Aerospace Sciences Meeting, Reno, NV, January 2006.

[22] Cybyk, B. Z., Grossman, K. R., Wilkerson, J. T., Chen, J., and Katz, J., "Single-Pulse Performance of the SparkJet Flow Control Actuator," AIAA Paper No. 05-0401, 43rd AIAA Aerospace Sciences Meeting, Reno, NV, January 2005.

[23] Anand, U., and Katz. J., "Prevention of Nozzle Wear in Abrasive Water Suspension Jets (AWSJ) Using Porous Lubricated Nozzles," *ASME J. of Tribology*, Vol. 125, 2003, pg. 168.

[24] Roth, G., and Katz, J., "Five Techniques for Increasing the Speed and Accuracy of PIV Interrogation," *Meas. Sci. Technol.*, Vol. 12, 2001, pg. 238.

[25] Sridhar, G., and Katz, J., "Lift and Drag Forces on Microscopic Bubbles Entrained by a Vortex," *Physics of Fluids*, Vol. 7, 1995, pg. 389.

[26] Roth, G., Mascenik, D. T., and Katz, J., "Measurements of the Flow Structure and Turbulence Within a Ship Bow Wave," *Physics of Fluids*, Vol. 11, 1999, pg. 3512.

[27] Alkislar, M., Choutapalli, I., and others, "The Structure of a Pulsed Jet – a PIV Study," AIAA Paper No. 05-1274, AIAA Fluid Dynamics Conference, Toronto, Ontario, Canada, June 2005.

[28] Cubbin, E. A., Ziemer, J. K., Choueiri, E. Y., and Jahn, R. G., "Pulsed Thrust Measurements using Laser Interferometry," *Review of Scientific Instruments*, Vol. 68, No. 6, June 1997.

[29] Sahu, J., "Unsteady CFD Modeling of Aerodynamic Flow Control Over a Spinning Body With Synthetic Jet," AIAA Paper No. 04-0747, 42nd AIAA Aerospace Sciences Meeting, Reno, NV, January 2004.